

Article

A Control Strategy for Achieving Constant Voltage Output with an Extensive ZVS Operating Range in Bidirectional Wireless EV Charging Systems

Guangyao Li ¹, Yafei Chen ², Hailong Zhang ³, Junchen Xie ¹, Seungjin Jo ¹ and Dong-Hee Kim ^{1,*}

¹ Department of Electrical Engineering, Chonnam National University, 77, Yongbong-ro, Buk-gu, Gwangju 61186, Republic of Korea; 206859@jnu.ac.kr (G.L.); 217916@jnu.ac.kr (J.X.); 206658@jnu.ac.kr (S.J.)

² College of Electrical and Information Engineering, Zhengzhou University of Light Industry, Zhengzhou 450002, China; swjtuqust@163.com

³ Department of Information and Control Engineering, Qingdao University of Technology, Qingdao 266525, China; zhanghailong@qut.edu.cn

* Correspondence: kimdonghee@jnu.ac.kr; Tel.: +82-62-530-1736

Abstract: Variations in the coupling coefficient of loosely coupled transformers and dynamic loads have a significant impact on the overall performance of bidirectional inductive power transfer (BIPT) systems. However, a wide range of load and coupling coefficient variations are common in the actual charging process, which may cause the converter on both sides to operate in a hard switching state, resulting in switching noise, reduced efficiency, and potential safety concerns. In this paper, a triple-phase-shift control (TPSC) strategy is proposed to study the zero-voltage switching (ZVS) operating range and constant-voltage output (CVO) characteristics of the double-side-LCC (DS-LCC) topology. To ensure a CVO over the wide range of coupling coefficient variations, a dual-phase-shift control is introduced for AC voltage matching. Based on this, the third phase-shift angle control between the converters on both sides is introduced to ensure the ZVS realization. Meanwhile, the time-domain model is developed to analyze the rationality of the proposed third phase-shift angle and the ZVS operating range. Finally, the effectiveness of the proposed TPSC strategy is validated through a 1.5 kW experimental prototype with an air gap of 100–150 mm.

Keywords: bidirectional inductive power transfer (BIPT); triple-phase-shift control (TPSC); constant-voltage output (CVO); battery charging; zero-voltage switching (ZVS)



Citation: Li, G.; Chen, Y.; Zhang, H.; Xie, J.; Jo, S.; Kim, D.-H. A Control Strategy for Achieving Constant Voltage Output with an Extensive ZVS Operating Range in Bidirectional Wireless EV Charging Systems. *Energies* **2024**, *17*, 1819. <https://doi.org/10.3390/en17081819>

Academic Editors: Alexandre De Bernardinis and Khaled Itani

Received: 6 March 2024

Revised: 29 March 2024

Accepted: 8 April 2024

Published: 10 April 2024



Copyright: © 2024 by the authors. Licensee MDPI, Basel, Switzerland. This article is an open access article distributed under the terms and conditions of the Creative Commons Attribution (CC BY) license (<https://creativecommons.org/licenses/by/4.0/>).

1. Introduction

Inductive power transfer (IPT) technology enables wireless power transfer between systems via utilizing magnetic field coupling without requiring a physical connection. In addition, due to its advantages of safety, convenience, and low maintenance cost [1–3], it may be applied in the fields of medical implants [4,5], household electric appliances, and groundwater devices [6]. More so, the adoption of IPT for the wireless charging of electric vehicles (EVs) is one of its most promising applications [7–9].

As the market penetration of EVs increases, the irregular charging of EVs will inevitably have a significant effect on the stability of the power grid. However, the development of bidirectional inductive power transfer (BIPT) technology offers a workable solution to this issue [10,11]. Meanwhile, since EVs simultaneously possess the characteristics of load and power supply, they can utilize the grid-to-vehicle (G2V) technology to absorb the peak-time electric energy, as well as the vehicle-to-grid (V2G) technology to fill the valleys with electric energy [12]. This feature facilitates the formation of a power system that combines the energy matching of electric vehicles and smart grids, which will consequently enhance the grid's operational effectiveness.

Interestingly, compared with traditional unidirectional power transfer (UIPT) systems, BIPT systems enable wireless power transfer in each direction between a power source

and a movable device through electromagnetic coupling [13]. Further, as the onboard side of the BIPT system, the electric vehicle has to play both the load and the source, which undoubtedly increases the control complexity of the system. In the traditional UIPT system, passive uncontrolled rectification is generally used on the receiving side, which cannot achieve dynamic load matching. Hence, this results in the inability of the system to achieve efficient transmission of high-power density within a wide range of load changes [14,15]. Moreover, when the coupling coefficient decreases due to large coil misalignments, it becomes relatively difficult to ensure a constant-voltage output (CVO) or constant-current output (CCO), especially by controlling the duty cycle of the transmitting-side inverter or inner phase shifting, limiting the controllable range of the system [16]. As a result, the active control of the receiving side becomes very necessary. Although the solution of cascaded DC-DC converters can achieve dynamic impedance matching and CVO or CCO, additional converters inevitably increase the cost, volume, and loss of the IPT system [17,18].

Furthermore, the application of dual-active bridges (DAB) provides new inspiration for addressing this issue [19–23]. This is performed by employing active rectifiers (AR) on the receiving side, which is also applicable to the BIPT systems. Additionally, the introduction of AR provides more controllable variables, which makes the control of the BIPT system more flexible. Meanwhile, double-phase-shift control (DPSC) is a suitable technique for power flow control. Specifically, by controlling the duty cycle or phase shift of the converters on both sides, the power flow amplitude can be adjusted to facilitate the seamless transition between G2V and V2G [24]. In addition, dynamic impedance matching may be achieved by regulating the phase shift or duty cycle between the receiving-side active half bridges to optimize system efficiency. For instance, in [25,26], a DAB phase-shift modulation strategy for efficiency optimization is proposed. More precisely, by appropriately selecting phase-shift angles for the converter of both sides, the BIPT system can achieve dynamic load matching and power regulation simultaneously. To simultaneously achieve AC voltage matching and ZVS operation of the converters on both sides in the BIPT system, a dual-side asymmetrical voltage cancellation control was proposed, and a comparative experiment with DPSC and TPSC was carried out in [27]. However, the majority of the above-mentioned system optimization control schemes focus on studying the output characteristics of low-order compensation topologies under CCO resonant conditions. There is limited research on the output performance of CVO resonance conditions using high-order double-side-LCC (DS-LCC) compensation topologies.

Due to its many advantages, the LCC compensation topology on both sides of the LCT enables more flexible and efficient power transfer, adapting to various power levels without incurring significant losses. DS-LCC compensation topology has been extensively studied in BIPT systems [9,16,24]. For example, Li et al. proposed a method for designing a DS-LCC topology that achieves both CCO and CVO over a wide coupling coefficient range by regulating the phase-shift angle on the transmitting side [16]. Vu et al. attempted a DS-LCC topology that possesses two independent resonant frequencies, allowing for the realization of both CCO and CVO through frequency control [28]. In another work, Chen et al. proposed a novel parameter-tuning method to optimize the DS-LCC compensated system's efficiency [29]. However, when the BIPT system terminates the CCO to perform the CVO operation, the CVO of the DS-LCC topology cannot ensure the output voltage stability over the range of load variation in the misalignment cases [16,29]. Furthermore, changes in mutual inductance can alter the resonance conditions within the resonant network, leading to a shift in the input zero-phase-angle (ZPA) and imposing ZVS challenges on the MOSFETs of the transmitting and receiving sides. Therefore, the DS-LCC topology plays a crucial role in the effectiveness of the TPSC strategy. The DS-LCC system using the TPSC strategy is more adaptable to different power needs, especially in terms of scalability for higher-power applications.

This study proposes a TPSC strategy for the BIPT systems to solve this problem. The main contributions of this paper are as follows:

- (1) Propose a TPSC strategy to study the ZVS operating range and CVO characteristics of the DS-LCC topology.
- (2) Establish a time domain model to analyze the rationality of the proposed third phase-shift angle and deduce the conditions for achieving ZVS.
- (3) The 1.5 kW experimental prototype verified that the proposed TPSC strategy could enable IPT to achieve efficient CVO under the misalignment tolerance of air gap 100–150 mm.

The remainder of this paper is organized as follows: In Section 2, the CVO characteristics of the DS-LCC topology are analyzed, and the effect of the TPSC on the DS-LCC topology is investigated. In Section 3, a time-domain model is realized, and the ZVS operating range of the MOSFETs is investigated over a wide coupling range. In Section 4, a comparative experiment between conventional DPSC and TPSC was conducted to verify the effectiveness of the proposed TPSC. Section 5 presents the conclusions.

2. Theoretical Analysis of the BIPT System

2.1. Analysis CVO Characteristic of DS-LCC Compensated BIPT System

Figure 1 shows the typical diagram of the DS-LCC compensated BIPT system, which includes two high-frequency FBI, a loosely coupled transformer (LCT), and a two-sided LCC resonant network. Precisely, the transmitting (receiving) side constitutes a DC-bus voltage U_{DC} (U_b), an AC voltage U_{AB} (U_{ab}), an inductor L_1 (L_2), a parallel capacitor C_{p1} (C_{p2}), a series capacitor C_{f1} (C_{f2}), and a self-inductance L_p (L_s). The transmitter and receiver are coupled by mutual inductances M . Additionally, the two sides are weakly coupled by magnetic induction through a large air gap (100–150 mm). Among them, the FBIs consist of eight power MOSFETs Q_1 – Q_8 , which are utilized to convert the DC-bus voltage to the AC voltage.

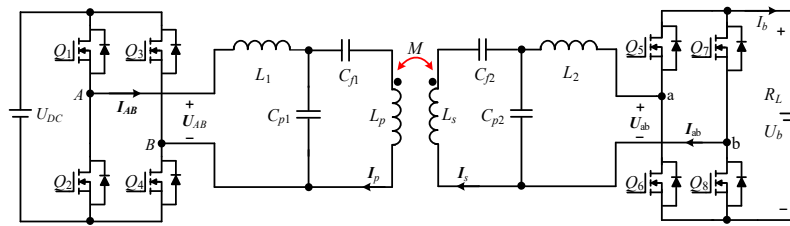


Figure 1. BIPT systems with DS-LCC compensation topology.

In general, the DS-LCC compensated BIPT system can achieve CCO with I_b as a constant and U_b as a variable that varies according to the time-varying battery load. However, by rationally designing compensation parameters, CVO can also be achieved through frequency control. Figure 2 shows the equivalent circuit of the DS-LCC compensation topology based on the T model. It depicts a further simplification of the analysis of the DS-LCC topology based on the CVO characteristics. Through LC resonant network, ZPA adjustment, π -type resonant network, and CL resonant network, CVO is finally realized [29]. In Figure 2, L_{se} is the equivalent inductance generated by L_{rs} and C_{f2} in series, which together with mutual inductance M and C_{p21} constitute a π -type resonant network, whose calculation method is $L_{se} = L_s - 1/(\omega_o^2 C_{f2})$.

The Kirchhoff's voltage law matrix equation of the CVO mode can be expressed as

$$\begin{bmatrix} U_{AB} \\ 0 \\ 0 \\ 0 \\ 0 \end{bmatrix} = \begin{bmatrix} jZ_a & \frac{j}{\omega C_{p1}} & 0 & 0 & 0 \\ \frac{j}{\omega C_{p1}} & jZ_d & -j\omega M & 0 & 0 \\ 0 & -j\omega M & jZ_e & \frac{j}{\omega C_{p21}} & 0 \\ 0 & 0 & \frac{j}{\omega C_{p21}} & jZ_c & \frac{j}{\omega C_{p22}} \\ 0 & 0 & 0 & \frac{j}{\omega C_{p22}} & jZ_b + R_{Leq} \end{bmatrix} \begin{bmatrix} I_{AB} \\ I_p \\ I_s \\ I_\pi \\ I_{ab} \end{bmatrix}. \quad (1)$$

where Z_a, Z_b, Z_c, Z_d , and Z_e can be expressed as

$$\begin{aligned} Z_a &= \omega L_1 - 1/(\omega C_{p1}), Z_b = \omega L_2 - 1/(\omega C_{p22}), Z_c = -1/(\omega C_{p21}) - 1/(\omega C_{p22}) \\ Z_d &= \omega M + \omega L_{rp} - 1/(\omega C_{f1}) - 1/(\omega C_{p1}), Z_e = \omega M + \omega L_{rs} - 1/(\omega C_{p21}) - 1/(\omega C_{f2}). \end{aligned} \quad (2)$$

where L_{rp} (L_{rs}) is the leakage inductance of the self-inductance L_p (L_s). U_{Lp} and U_{Ls} represent the induced voltages in the transmitting and receiving coils, respectively, which may be expressed as

$$U_{Lp} = -j\omega M I_s, U_{Ls} = -j\omega M I_p. \quad (3)$$

where M is the mutual inductance of the LCT, and the coupling coefficient k can be calculated as

$$k = M/\sqrt{L_p L_s} \quad (4)$$

The resonant angular frequency ω_0 is determined, based on the self-inductance of the coupler coils, to be independent of the misalignment between the two sides during the operation as

$$\begin{aligned} \omega_0 &= 1/\sqrt{L_1 C_{p1}} = 1/\sqrt{L_{se} C_{p21}} = 1/\sqrt{L_2 C_{p22}} \\ &= \sqrt{C_{p22} L_{se} / (C_{f1} (C_{p22} L_{se} (L_p - L_1) - M^2 C_{p2}))}. \end{aligned} \quad (5)$$

where $C_{p2} = C_{p21} + C_{p22}$ [29].

Because C_{f1} plays a role in ZPA adjustment, as shown in Figure 2, it can be seen from (5) that the increase of M will lead to the increase of C_{f1} to meet the ZPA condition of the BIPT system. However, in practical applications, once the compensation parameters of the BIPT system are designed, the parameters in the resonance tank usually cannot be changed, which will inevitably affect the system performance in the misalignment case.

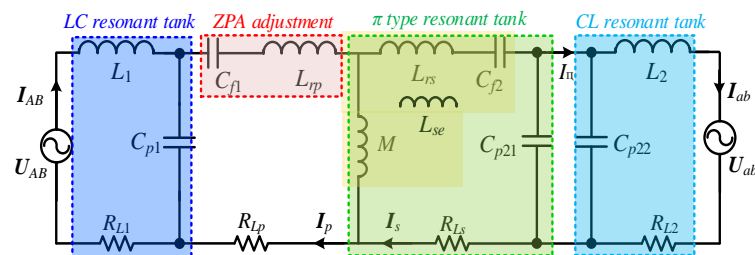


Figure 2. Equivalent circuit for the DS-LCC compensation topology based on the T-type model.

Furthermore, the system input impedance Z_{in} and the input phase angle θ_{in} of the BIPT system can be expressed as

$$\begin{cases} Z_{in} = j\omega L_1 + \frac{1}{j\omega C_{p1}} \parallel (j\omega L_p + \frac{1}{j\omega C_{f1}} + \frac{\omega^2 M^2}{Z_s}) \\ \theta_{in} = \frac{180^\circ}{\pi} \arctan \frac{Im(Z_{in})}{Re(Z_{in})}. \end{cases} \quad (6)$$

where the symbol “ \parallel ” expresses the parallel connection. Z_s is the impedance of the receiving side by $Z_s = j\omega L_s - j/(\omega C_{f2}) - j/(\omega C_{p2}) \parallel (j\omega L_2 + R_{Leq})$.

By substituting the resonance condition (5) into the matrix Equation (1), the CVO operating at the resonance point regardless of the load variation can be determined as

$$U_{ab} = -\frac{M L_2 U_{AB}}{L_1 L_{se}}. \quad (7)$$

According to (7), the input voltage U_{ab} of the receiving-side inverter lags behind the U_{AB} of the transmitting side inverter by 180° and varies with the variation of M .

By utilizing (6) and (7), the Bode diagram of the input phase angle and voltage gain is obtained under different coupling coefficients k , as shown in Figure 3. It can be seen that the

input phase angle of the BIPT system is affected by the change of k . The input phase angle increases with the increase of the load at the resonant frequency of 85 kHz with $k = 0.237$, and the ZPA condition cannot be satisfied, which is the reason for the ZVS challenge of the MOSFETs of the converter. Meanwhile, it is not difficult to find that the voltage gain of the system changes as k increases, which makes the system lose its CVO characteristics.

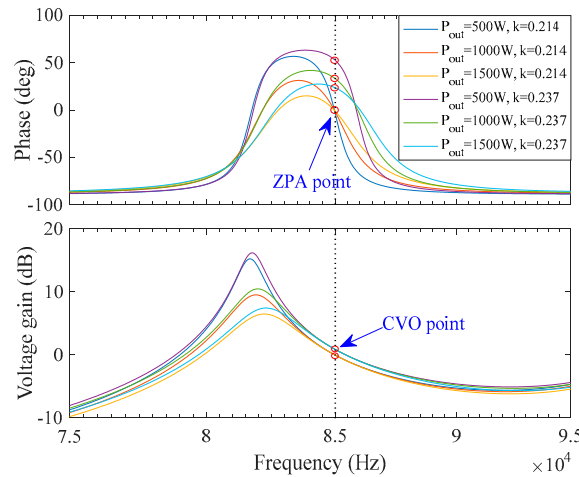


Figure 3. Bode diagram of the BIPT system under alignment and misalignment situation.

Therefore, in order to make the BIPT system realize the CVO feature with ZPA condition in the misaligned cases, it is possible to control the third phase-shift angle between the full bridges of the transmitting- and receiving-side converters, as well as the phase-shift angles between the two half bridges of each side’s converter. In this way, the AC voltage U_{AB} (U_{ab}) of the transmitting and receiving sides and input phase angle will be controlled. This will be analyzed in detail in the following section.

2.2. Influence of DPSC Strategy for the AC Voltage Matching of DS-LCC Compensated Topology

Generally, the FBIs of both the transmitting and receiving sides generate periodic square voltages (U_{AB} and U_{ab}) with a duty cycle, which are described using Fourier series analysis [30]. In terms of the switching resonance angular frequency ω_o , the square wave voltage generated by FBI and AR can be expanded using a Fourier series.

$$\begin{aligned}
 U_{AB} &= \frac{4}{\pi} U_{DC} \sum_{n=1,3,\dots}^{\infty} \frac{1}{n} \cos(n\omega_o t - \frac{n\alpha}{2}) \sin \frac{n\alpha}{2} \\
 U_{ab} &= \frac{4}{\pi} U_b \sum_{n=1,3,\dots}^{\infty} \frac{1}{n} \cos(n\omega_o t - \frac{n\alpha}{2} + n\delta) \sin \frac{n\beta}{2}.
 \end{aligned}
 \tag{8}$$

where the drive signals of the MOSFETs and the output voltage U_{AB} and input voltage U_{ab} on both sides’ converter are shown in Figure 4.

The upper and lower bridge arms are turned on alternately with a duty cycle of 0.5 at an operating frequency of 85 kHz. Q_3 turns on ahead of Q_1 by a phase angle α , and Q_7 turns on ahead of Q_5 by a phase angle β . δ is the third phase-shift angle between U_{AB} and U_{ab} . For synchronous control between converters on both sides, the auxiliary winding method can be utilized to achieve synchronous control [31], where n is the number of harmonics. Specifically, the fundamental harmonic analysis (FHA) method is widely used for qualitative analysis by considering the harmonic suppression of higher-order resonant networks in a BIPT system; hence, $n = 1$ in this paper. So, (8) can be rewritten as

$$U_{AB}(t) = \frac{4U_{DC}}{\pi} \sin \frac{\alpha}{2} \cos(\omega_o t), \quad U_{ab}(t) = \frac{4U_b}{\pi} \sin \frac{\beta}{2} \cos(\omega_o t + \delta).
 \tag{9}$$

Figure 4 shows the phase-shift switching sequence for the DS-LCC topology to realize the CVO. Specifically, the phase-shift angle α is utilized to modulate the AC output voltage magnitude of the FBI of the transmitting side, and β is utilized to modulate the AC input voltage magnitude of receiving-side AR. Meanwhile, δ typically determines the control of power flow to charge or discharge the EVs and to switch between the various modes of operation. When δ is negative, power flows from the transmitting side to the receiving side for charging the EVs (G2V). Conversely, when δ is positive, power can be transferred from the receiving side to the transmitting side to supply power to the grid (V2G). In Figure 4, the dead time accounts for a small proportion, which is not considered in the figure, but it is considered in the actual experiment of this paper.

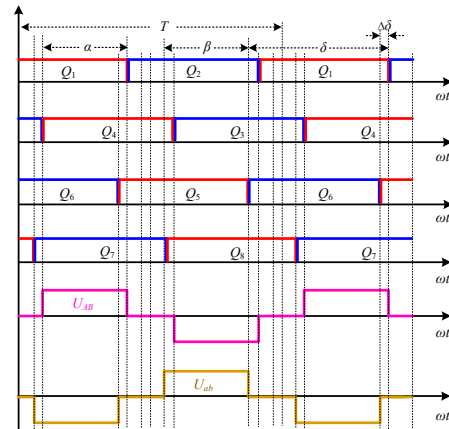


Figure 4. Switching sequence of phase-shift control in the BIPT system.

Under the premise of satisfying the resonance condition and neglecting the resistive losses, based on the underlying power flow equation and KVL, the active power P and reactive power Q of BIPT systems are described as

$$\begin{aligned}
 P &= -\frac{8M}{\pi^2\omega_0 L_1 L_2} \sqrt{\frac{L_p}{L_s}} U_{DC} U_b \sin\left(\frac{\alpha}{2}\right) \sin\left(\frac{\beta}{2}\right) \cos(\delta), \\
 Q &= -\frac{8M}{\pi^2\omega_0 L_1 L_2} \sqrt{\frac{L_p}{L_s}} U_{DC} U_b \sin\left(\frac{\alpha}{2}\right) \sin\left(\frac{\beta}{2}\right) \sin(\delta).
 \end{aligned}
 \tag{10}$$

The power flow is a function of the control parameters α , β , and δ of the transmitter-side and receiver-side converters. To further illustrate the functional relationship, Figure 5 depicts a three-dimensional plot of the variation of output power according to phase-shift angles. It can be observed that the output power exhibits a nonlinear monotonic increase as α and β increase. Further, to maximize power transfer and achieve relatively high system efficiency, it can be seen that the phase-shift angles α and β can be controlled to achieve AC voltage matching. Meanwhile, the third phase-shift angle δ is typically set to $\pm 180^\circ$ to minimize reactive power flow and achieve a unity power factor operation.

The DC voltage gain G_{DC} (AC voltage gain G_{ac}) of the receiving-side converter's output voltage (input voltage) and the transmitting-side converter's input voltage (output voltage), respectively, can be expressed as

$$G_{DC} = \frac{U_b}{U_{DC}} \quad G_{ac} = \frac{U_{ab}}{U_{AB}}.
 \tag{11}$$

By substituting (9) into (11), the relationship between the phase-shift angle α , β , and G_{ac} can be expressed as

$$G_{ac} = G_{DC} \frac{\sin(\beta/2)}{\sin(\alpha/2)}.
 \tag{12}$$

As can be noticed in (12), α and β are a function of G_{ac} when δ is 0. To remain G_{DC} constant and achieve the AC voltage matching, by substituting (10) and (11) into (12), the desired α and β for a given active output power P can be derived as

$$\alpha = 2\arcsin\left(\frac{\sqrt{2}\pi}{4U_{DC}}\sqrt{\frac{P\omega_0 L_1 L_2 \sqrt{L_s}}{M\sqrt{L_p} G_{ac}}}\right), \beta = 2\arcsin\left(\frac{\sqrt{2}\pi}{4U_b}\sqrt{\frac{P\omega_0 L_1 L_2 \sqrt{L_s} G_{ac}}{M\sqrt{L_p}}}\right). \quad (13)$$

As shown in (13), once the DC-bus voltages on both sides and the system design parameters have been determined, the phase-shift angles α and β have a monotonic relationship with the AC voltage gain G_{ac} , allowing the possibility for straightforward control.

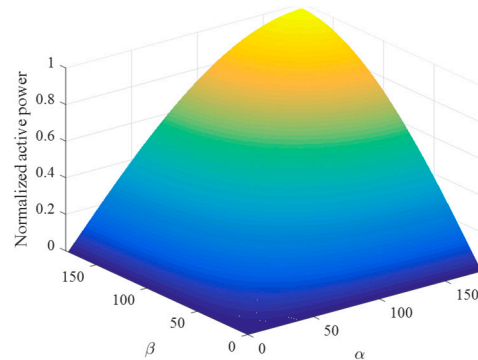


Figure 5. Normalized active power varies with the phase-shift angles α and β .

Figure 6 shows the relationship between α and β according to different AC voltage gains. Under the premise of ensuring the DC voltage gain $G_{DC} = 1$, different G_{ac} correspond to different M . Precisely, when $G_{ac} > 1$, it means that M increases, the absolute value of the AC voltage gain will increase, and the change of the β phase-shift angle is higher than that of α . Meanwhile, when $G_{ac} < 1$, it indicates that M decreases, and the change of α angle is higher than β so as to ensure that the BIPT system output voltage remains unchanged.

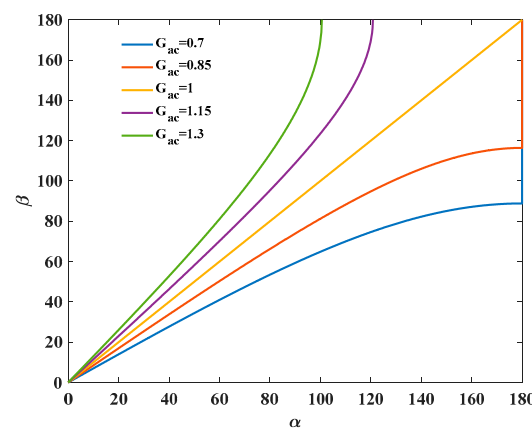


Figure 6. Relationship between α and β according to different AC voltage gains G_{ac} .

2.3. Analysis of the Influence of Third Phase-Shift δ on the AC Efficiency of the BIPT System

In the BIPT system, the total power loss includes losses such as the core loss and copper loss of the LCT and the two compensation inductors, the conductive loss and the diode loss of the FBI and AR, capacitor loss, and some other stray loss. In this section, the main objective is to analyze the influence of the third phase-shift angle δ on the AC efficiency of the system. If δ has little effect on the AC system efficiency, it becomes reasonable to compare the effect of δ on the losses of the converters on both sides. Therefore, only the copper loss of the LCT and the two compensation inductors in the resonant tank are

modeled and analyzed. Assuming that the system parameters are symmetrical, let $L_p = L_s$, $L_1 = L_2$, $R_{12} = R_{L1} = R_{L2}$, and $R = R_{Lp} = R_{Ls}$, the total loss can be calculated as

$$P_{Loss} = I_{AB}^2 R_{L1} + I_p^2 R_{Lp} + I_{ab}^2 R_{L2} + I_s^2 R_{Ls}. \quad (14)$$

The system AC efficiency can be determined by

$$\eta = \frac{P}{P + P_{Loss}}. \quad (15)$$

According to (1), the I_p and I_s can be represented as

$$I_p = \frac{U_{AB}}{j\omega L_1}, \quad I_s = U_{ab} A. \quad (16)$$

The relationship between the DC load resistor R_L and the AC equivalent load resistor R_{Leq} can be represented by

$$R_{Leq} = \frac{8}{\pi^2} \sin^2\left(\frac{\beta}{2}\right) R_L. \quad (17)$$

By substituting (1), (10), and (14) into (15), the approximate system AC efficiency can be deduced as

$$\eta \approx \frac{M/(\omega L_1^2) |\cos(\delta)|}{\frac{M|\cos(\delta)|}{(\omega L_1^2)} + (G_{ac} + \frac{1}{G_{ac}}) \frac{M^2 A^2}{L_1^2} R_{12} + (\frac{1}{\omega^2 L_1^2 G_{ac}} + G_{ac} A^2) R}. \quad (18)$$

where $A^2 = (L_2/R_{Leq}L_{se})^2 + 1/\omega_0^2(1/L_2 + 1/L_{se})^2$ [29].

Noting that the BIPT system operates in CVO mode with a relatively high load, “A” can be considered constant under such conditions. According to the designed system compensation parameters, as shown in Tables 1 and 2 in Section 4, A^2 is approximately equal to 0.0183.

Table 1. Essential system parameters of the BIPT system.

Symbols	Parameters	Values
U_{DC}	DC-link input voltage	220 V
f_o	Resonant frequency	85 kHz
P_o	Rate output power	1.5 kW
U_b	Battery charging voltage	220 V
k	Coupling coefficient	0.16–0.25
M	Mutual inductance	18.0–27.9 μ H
L_p	Transmitting-coil self-inductance	111.17 μ H
L_s	Receiving-coil self-inductance	112.66 μ H

Table 2. Designed parameters of the proposed BIPT system.

Symbols	Parameters	Values
L_1	Transmitting-side compensation inductance	34.6 μ H
L_2	Receiving-side compensation inductance	34.6 μ H
C_{p1}	Transmitting-side compensated capacitance	101.4 nF
C_{p2}	Receiving-side parallel compensation capacitance	247.7 nF
C_{f1}	Transmitting-side series compensation capacitance	194.2 nF
C_{f2}	Receiving-side series compensation capacitance	39.5 nF

In addition, maximum system AC efficiency is achieved by solving the derivative of the system's efficiency based on the AC voltage gains G_{ac} , which can be written as

$$\frac{d\eta}{dG_{ac}} = 0 \Rightarrow G_{ac} = 0.845. \quad (19)$$

According to (19), let the derivative be equal to zero, the maximum system efficiency is achieved when the optimal AC voltage gain is 0.845. Under the optimal AC voltage gain, the maximum BIPT system efficiency can be rewritten as

$$\eta_{\max} \approx \frac{M/(\omega L_1^2) |\cos(\delta)|}{\frac{M|\cos(\delta)|}{(\omega L_1^2)} + \frac{0.037M^2}{L_1^2} R_{12} + \left(\frac{1.1834}{\omega^2 L_1^2} + 0.0154\right) R}. \quad (20)$$

According to (18) and Figure 7, it can be seen that the AC system efficiency varies with G_{ac} and δ . It can be observed that the AC system efficiency increases with the increase of G_{ac} until it reaches the maximum efficiency and then gradually decreases steadily, while the system efficiency decreases with the decrease of the third phase-shift angle δ . In particular, it is found that when G_{ac} is around 0.845, a small δ change has little effect on the AC system efficiency, but when δ deviates greatly from 180° , the AC system efficiency decreases significantly.

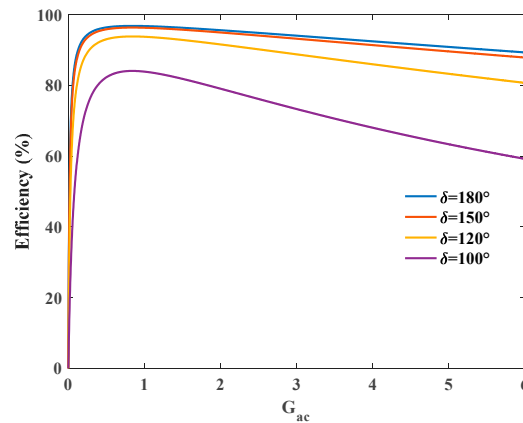


Figure 7. Efficiency of BIPT systems against G_{ac} and δ .

3. Establishment of Time Domain Model and Realization of ZVS

As mentioned in the previous section, the BIPT systems can be controlled through DPSC. However, the adjustment of the ZVS operating range of the converters on both sides is limited by the conventional DPSC strategy, especially when the nonlinearity of the load increases or the LCT under the misalignment case. This will change the input impedance phase angle of the DS-LCC topology so that the converters on both sides may not all work under the condition of ZVS.

The TPSC strategy is proposed in this section to reduce the switching loss caused by the hard switching of MOSFETs. Consistent with ensuring maximum system efficiency, the third phase-shift angle δ is slightly adjusted to generate hysteresis current to achieve the soft switching of MOSFETs and establish a time-domain model based on the fundamental harmonics approximation method to analyze the proposed TPSC strategy.

3.1. Establishment of Time-Domain Model of BIPT Systems

It is necessary to perform a time-domain modeling analysis on the current and terminal voltage flowing through the converters on both sides to determine the ZVS operating range of both sides' converters. Meanwhile, to simplify the analysis, the influence of the coil resistance on the current is ignored in the model, and the simplified M -model of the BIPT system is shown in Figure 8.

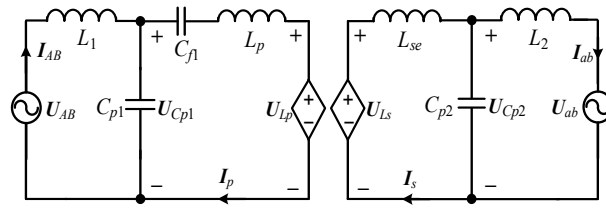


Figure 8. Simplified BIPT system based on the M -model.

In particular, since the voltage transfer functions of the BIPT systems in the G2V and V2G directions are reciprocal and symmetrical, only the G2V direction is analyzed. Considering the sum of the phase-shift angle π corresponding to the maximum power transmission point and the introduced phase-shift compensation angle $\Delta\delta$ as the third phase-shift angle δ , it can be expressed as

$$\delta = \pi + \Delta\delta. \quad (21)$$

In addition, because the DS-LCC compensation topology is a high-order and can filter out the high-frequency harmonics in the BIPT systems, the FHA model is used to calculate the coil current, which can be expressed as

$$I_p(t) = \frac{4U_{DC}}{\pi\omega L_1} \sin \frac{\alpha}{2} \sin\left(\omega t - \frac{\pi}{2}\right). \quad (22)$$

$$I_s(t) = -\frac{4U_b A}{\pi} \sin \frac{\beta}{2} \sin\left(\omega t - \frac{\pi}{2} - \Delta\delta\right). \quad (23)$$

U_{Lp} and U_{Ls} are the coil-induced voltage of the transmitting and receiving sides that are induced by I_p and I_s , as shown in (3). With the losses neglected, the voltage across C_{p1} is equal to the sum of U_{Lp} and the voltage throughout L_p and C_{f1} can be expressed as

$$U_{Cp1} = -j\omega M I_s + (j\omega L_p + 1/(j\omega C_{f1}))I_p. \quad (24)$$

Therefore, by substituting (3) and (22) into (24), the time-domain expression of U_{Cp1} can be rewritten as

$$U_{Cp1}(t) = \frac{4U_b\omega M A}{\pi} \sin \frac{\beta}{2} \sin(\omega t - \Delta\delta) + \frac{4U_{DC}}{\pi} \sin \frac{\alpha}{2} \sin(\omega t). \quad (25)$$

Similarly, the time-domain expression of U_{Cp2} on the receiving side can be shown as

$$U_{Cp2}(t) = \frac{4U_{DC}M}{\pi L_1} \sin \frac{\alpha}{2} \sin(\omega t) + \frac{4U_b\omega L_{se}A}{\pi} \sin \frac{\beta}{2} \sin(\omega t - \Delta\delta). \quad (26)$$

The essential operating waveforms of the simplified circuit model are illustrated in Figure 9. Additionally, the circuit mode can be described with a differential equation on the transmitting side, which can be expressed as

$$U_{AB}(t) - U_{Cp1}(t) = L_1 \frac{dI_{L1}(t)}{dt}. \quad (27)$$

Substituting (9) and (25) into (27) and then integrating (27), the expression for the output current of the inverter on the transmitting side can be obtained as

$$I_{L1}(t) = \frac{1}{\omega L_1} \int_0^t \left[\frac{4U_{DC}}{\pi} \sin \frac{\alpha}{2} \cos\left(\omega t - \frac{\pi}{2}\right) + \frac{4U_b\omega M A}{\pi} \sin \frac{\beta}{2} \sin(\omega t - \Delta\delta) - \frac{4U_{DC}}{\pi} \sin \frac{\alpha}{2} \sin(\omega t) \right] d(\omega t). \quad (28)$$

By solving the differential equation, the output currents of the transmitter side’s inverter at the times $t_0, t_1,$ and t_2 shown in Figure 9 are expressed as

$$I_{L1}(\omega t_0 = 0) = -\frac{\alpha U_{DC}}{2\omega L_1} - \frac{4U_b MA}{\pi L_1} \sin \frac{\beta}{2} \sin(\Delta\delta) + \frac{4U_{DC}}{\pi\omega L_1} \sin\left(\frac{\alpha}{2}\right) \quad (29)$$

$$I_{L1}(\omega t_1 = \frac{\pi - \alpha}{2}) = -\frac{\alpha U_{DC}}{2\omega L_1} - \frac{4U_b MA}{\pi L_1} \sin \frac{\beta}{2} \sin\left(\frac{\alpha}{2} + \Delta\delta\right) + \frac{4U_{DC}}{\pi\omega L_1} \sin^2\left(\frac{\alpha}{2}\right) \quad (30)$$

$$I_{L1}(\omega t_2 = \frac{\pi + \alpha}{2}) = \frac{\alpha U_{DC}}{2\omega L_1} + \frac{4U_b MA}{\pi L_1} \sin \frac{\beta}{2} \sin\left(\frac{\alpha}{2} - \Delta\delta\right) - \frac{4U_{DC}}{\pi\omega L_1} \sin^2\left(\frac{\alpha}{2}\right). \quad (31)$$

Because the time-domain model of the current has symmetry in the positive and negative half-cycles, only the positive half-cycles are analyzed in this section. In addition, it is obvious that the current at time t_3 can be expressed as

$$I_{L1}(\omega t_3) = -I_{L1}(\omega t_0 = 0). \quad (32)$$

Similarly, the differential equation of the output current on the receiving side can be expressed as

$$U_{ab}(t) - U_{Cp2}(t) = L_2 \frac{dI_{L2}(t)}{dt}. \quad (33)$$

In addition, the expression for the input current of the AR on the receiving side can be obtained as

$$I_{L2}(t) = \frac{1}{\omega L_2} \int_{t_7}^t \left\{ \frac{4U_b}{\pi} \sin \frac{\beta}{2} \cos(\omega t - \frac{\pi}{2} - \delta) - \frac{4U_{DC}M}{\pi L_1} \sin \frac{\alpha}{2} \sin(\omega t) + \frac{4U_b \omega L_{se}A}{\pi} \sin \frac{\beta}{2} \sin(\omega t - \Delta\delta) \right\} d(\omega t). \quad (34)$$

The input currents of the receiving side’s AR at the times $t_4, t_5, t_6,$ and t_7 shown in Figure 9 are expressed as

$$I_{L2}(\omega t_7 = \Delta\delta) = -\frac{4MU_{DC}}{\pi L_2} \sin \frac{\alpha}{2} \cos(\Delta\delta). \quad (35)$$

$$I_{L2}(\omega t_8 = \frac{\pi - \beta}{2} + \Delta\delta) = -\frac{U_b \beta}{2\omega L_2} + \frac{4U_{DC}M}{\pi L_2} \sin\left(\frac{\beta}{2} - \Delta\delta\right) \sin\left(\frac{\alpha}{2}\right) - \frac{4U_b L_{se}A}{L_2 \pi} \sin^2\left(\frac{\beta}{2}\right). \quad (36)$$

$$I_{L2}(\omega t_9 = \frac{\pi + \beta}{2} + \Delta\delta) = \frac{U_b \beta}{2\omega L_2} - \frac{4U_{DC}M}{\pi L_2} \sin\left(\frac{\beta}{2} + \Delta\delta\right) \sin\left(\frac{\alpha}{2}\right) + \frac{4U_b L_{se}A}{\pi L_2} \sin^2\left(\frac{\beta}{2}\right). \quad (37)$$

$$I_{L2}(\omega t_{10}) = -I_{L2}(\omega t_7 = \Delta\delta). \quad (38)$$

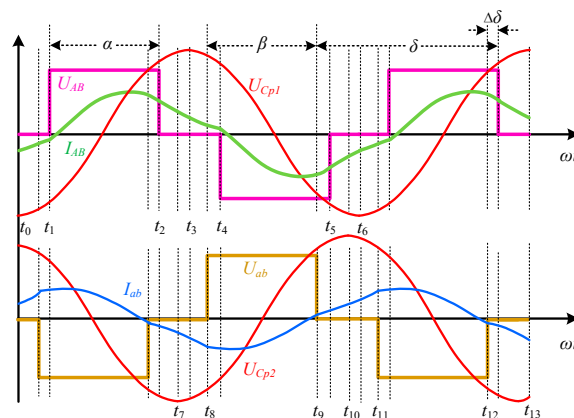


Figure 9. Essential operating waveforms of the BIPT system with TPSC.

3.2. Realization of Extending the ZVS Operating Range

The ZVS operating range is obtained by ensuring that power switches turn ON with the drain-source voltage clamped to zero by conducting the antiparallel diode. To ensure ZVS for the MOSFETs of both sides, the following constraints should be satisfied.

$$\begin{aligned} I_{L1}(\omega t_1) < 0, I_{L1}(\omega t_2) > 0, I_{L1}(\omega t_4) > 0, I_{L1}(\omega t_5) < 0, \\ I_{L2}(\omega t_8) < 0, I_{L2}(\omega t_9) > 0, I_{L2}(\omega t_{11}) > 0, I_{L2}(\omega t_{12}) < 0. \end{aligned} \quad (39)$$

According to the symmetry of the current waveform, ZVS can only be realized if the sum of the currents at t_1 and t_2 is greater than 0. By combining (30) and (31), it can be obtained that

$$I_{L1}(t_1) + I_{L1}(t_2) = \frac{4U_b MA}{\pi L_1} \sin \frac{\beta}{2} (\sin(\frac{\alpha}{2} - \Delta\delta) - \sin(\frac{\alpha}{2} + \Delta\delta)) > 0. \quad (40)$$

It can be seen from the above equations that the inverter on the transmitting side can work in ZVS operation only if the current at time t_1 is less than 0. Similarly, only when the current at time t_8 is less than 0 can the receiving side AR work in the ZVS operation. Therefore, the conditions for the converters on both sides of the BIPT system to realize ZVS are

$$I_{L1}(\omega t_1) < 0, I_{L2}(\omega t_8) < 0. \quad (41)$$

Further, the ZVS operating ranges of the transmitting and receiving sides switches with $\Delta\delta = 0$ are shown in Figure 10, and the AC voltage gain ratio G_{ac} is 1. Precisely, the blue dotted lines are the trajectories of α and β under the AC voltage control strategy proposed in the previous section, as shown in Figure 6. Additionally, it can be seen that the ZVS operation range is relatively narrow. Only α and β are big. That is, at light load, the switches on the transmitting side can achieve ZVS. At medium load and heavy load, half of the switches of the inverters on both sides are in the hard switching state.

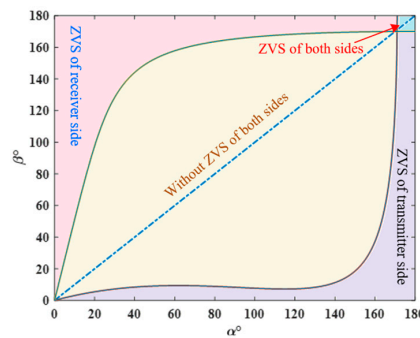


Figure 10. ZVS range of transmitting and receiving sides switches with $\Delta\delta = 0$.

Meanwhile, from (10), if U_{ab} lags U_{AB} by more than 180° , that is, $\Delta\delta > 0$, positive reactive power is generated so that an inductive impedance is inserted in the BIPT system to generate an inductive current. Specifically, inverters with inductive impedance are more likely to work in soft switching states. Conversely, if the system input impedance is inductive, $\Delta\delta < 0$ can be set to generate capacitive impedance to offset inductive impedance. More so, a slight shift of δ around $\pm 180^\circ$ has little effect on the system efficiency, as shown in Figure 7, which means that a smaller $\Delta\delta$ can be controlled to achieve ZVS without significantly affecting the system efficiency.

Figure 11 shows the ZVS operating ranges of all MOSFETs at the transmitting and receiving sides at different $\Delta\delta$ when the AC voltage ratio is $G_{ac} = 1$. Precisely, when $\Delta\delta = 0^\circ$, the critical curves of α and β intersect at the point (175, 175), and the whole coordinate system is decomposed into four different functional areas: the pink area represents that the receiving side can achieve ZVS, while the purple area represents ZVS operation achievement at the transmitting side. Furthermore, the blue area indicates that ZVS operation can

be achieved on both sides, whereas the yellow area indicates that ZVS operation cannot be achieved on both sides. However, with the increase of $\Delta\delta$, it can be clearly seen that the intersection points of the α and β critical curves gradually move to the lower left, and the blue area on both sides where ZVS operation can be achieved increases, while the yellow area where ZVS operation cannot be achieved decreases. This indicates that the operating range of ZVS can be increased by controlling the phase-shift compensation angle $\Delta\delta$ of the inverters on both sides. Specifically, when $\Delta\delta = 40^\circ$, the entire blue line is in the blue area. That is, the ZVS operating range of the entire power supply within a certain coupling coefficient variation range can be realized.

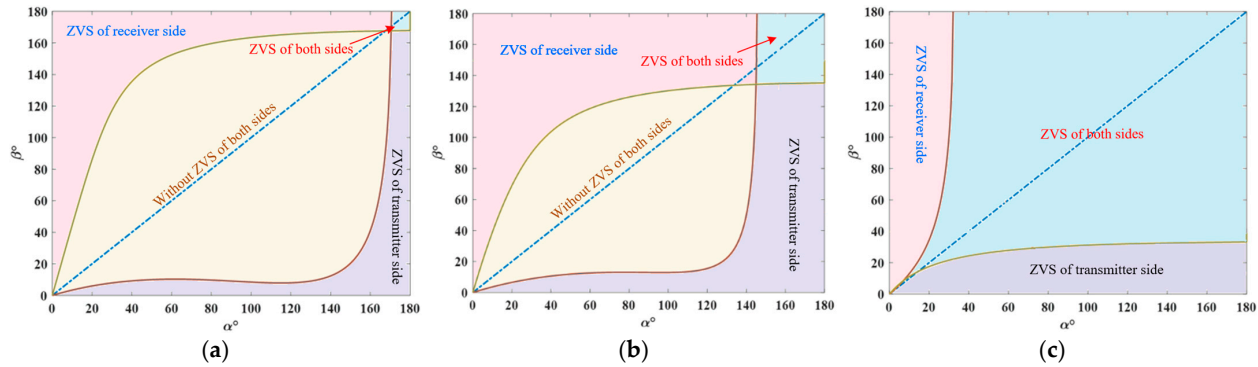


Figure 11. ZVS operating range of transmitter and receiver sides' MOSFETs under voltage gain $G_{DC} = 1$ with (a) $\Delta\delta = 0^\circ$, (b) $\Delta\delta = 10^\circ$, and (c) $\Delta\delta = 40^\circ$.

Therefore, under the premise of ensuring the minimum reactive power input, according to the discharge current I_d and the ZVS requirements, the optimal phase-shift compensation angle $\Delta\delta$ can be derived as

$$\Delta\delta = -\frac{\alpha}{2} + \arcsin\left(\frac{8U_{DC} \sin^2 \frac{\alpha}{2} - \alpha\pi U_{DC} - 2\pi I_d \omega L_1}{8\omega M U_b A \sin \frac{\beta}{2}}\right). \quad (42)$$

The optimal $\Delta\delta$ under different mutual inductance M is shown in Equation (42), which is the ideal case without considering the parallel parasitic capacitance of the switches, and the different I_d when considering the parallel parasitic capacitance are discussed. It can be seen that the compensated phase angle $\Delta\delta$ varies with the output voltage U_b and different M . Under ideal conditions, no or little compensation is required for $\Delta\delta$ under light loads. However, larger $\Delta\delta$ is required under heavy loads. When considering parallel parasitic capacitance, the necessary $\Delta\delta$ increases over the entire power range, especially under heavy loads. This is because the full bridge output current is small at heavy loads, so a larger $\Delta\delta$ is required to generate enough current to release the parasitic capacitor. Taking into account the different M , in an ideal case, the smaller M , the smaller the compensation angle required.

4. Experimental Verification

To verify the results of the theoretical analysis of the aforementioned TPSC model, a 1.5 kW experimental prototype was established according to the circuit diagram, as shown in Figure 12. According to the resonance condition (5), a set of BIPT system parameters is formulated, as listed in Table 1. Moreover, a set of resonance parameters of the DS-LCC compensation topology are calculated, as listed in Table 2. Among them, the control board uses DSP TMS320F28335. The switching devices employed are $Q_1 - Q_8 = C2M0080120D$. The power and DC/DC efficiency analysis of the BIPT system was performed using a digital power analyzer (HIOKI PW6001). The entire system was powered by a DC power source (LAB-DSP 350-08.4). To evaluate the performance of the CVO, an electronic load (IT8816B) was employed.

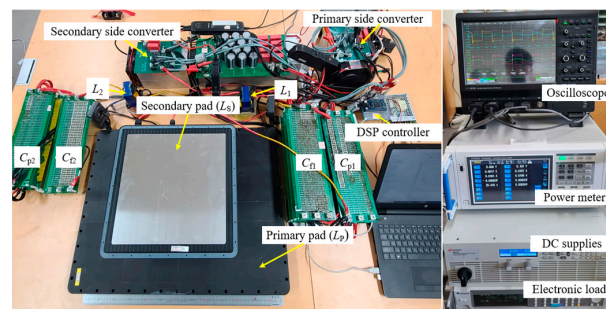


Figure 12. Experimental photograph of the BIPT system.

As shown in Figure 13, the LCT is designed and fulfills the SAEJ 2954 recommended standard. Additionally, the FBI and AR are constructed utilizing eight SiC power MOSFETs (C3M0030090K). In particular, a digital signal processor (DSP TMS320F28335) is adopted as the controller to generate driving signals for the eight MOSFETs.

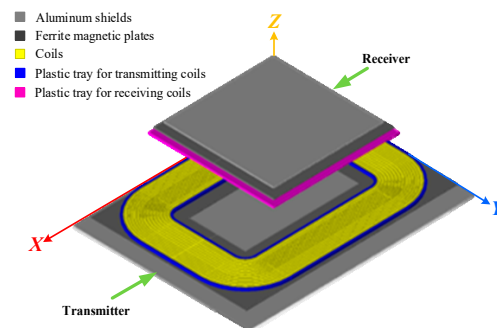


Figure 13. Three-dimensional LCT pad geometric structure design of BIPT system.

Furthermore, to verify the effectiveness of the proposed TPSC strategy, a comparative experiment of the conventional DPSC strategy is introduced. Figure 14 shows the voltage and current waveforms of the converter at the transmitting and receiving sides under $G_{ac} = 1$ and $k = 0.216$. On the premise that the DC voltage gain remains unchanged, only the conventional DPSC strategy is introduced to realize the AC voltage matching, and the third phase-shift angle δ between the transmitter and receiver converters is kept at -180° . Precisely, when the BIPT system works under full load, set $\alpha = \beta = 120^\circ$, it can be seen that with the DPS control strategy, only half of the MOSFETs can achieve ZVS, and the other half works in the hard switching state, which increases the loss of the BIPT system to a certain extent. From the voltage waveforms of the MOSFETs, it is found that there are spike voltages, which may destroy MOSFETs.

It is worth noting from Figure 14 that the voltage waveforms of the transmitting and receiving sides do not strictly maintain a phase-shift difference of -180° , and the β of the receiving side is slightly larger than α , which may be caused by the non-negligible dead time.

Thus, the proposed TPSC strategy was introduced into the BIPT system, and the output current and voltage waveforms were respectively given for light, medium, and full load with $\alpha = \beta = 180^\circ$, $\alpha = \beta = 150^\circ$, and $\alpha = \beta = 120^\circ$ when $k = 0.216$ and $G_{ac} = 1$, as shown in Figure 15. In addition, it can be seen that the MOSFETs of both sides can achieve ZVS switching within a wide load variation range. Specifically, the output current of the transmitting and receiving sides of the full-bridge converters at the switching point is negative. More so, the compensation angle $\Delta\delta$ can reach 12° under full load. This is because the output current is very small, and the output capacitance of the MOSFETs is large under full load. Therefore, a large compensation phase angle $\Delta\delta$ is injected into the system to fully discharge the capacitor by using the induced current generated.

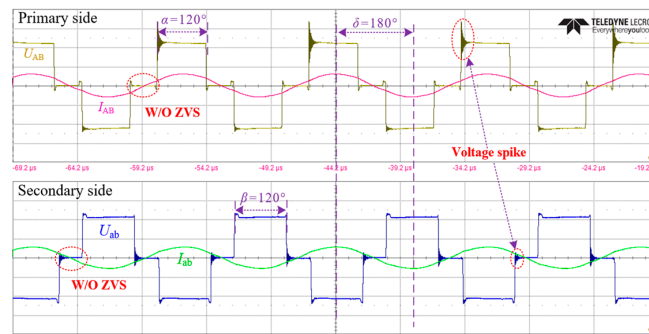


Figure 14. Voltage and current waveforms of the transmitter and receiver inverters with the conventional DPSC under $k = 0.216$ and $G_{ac} = 1$.

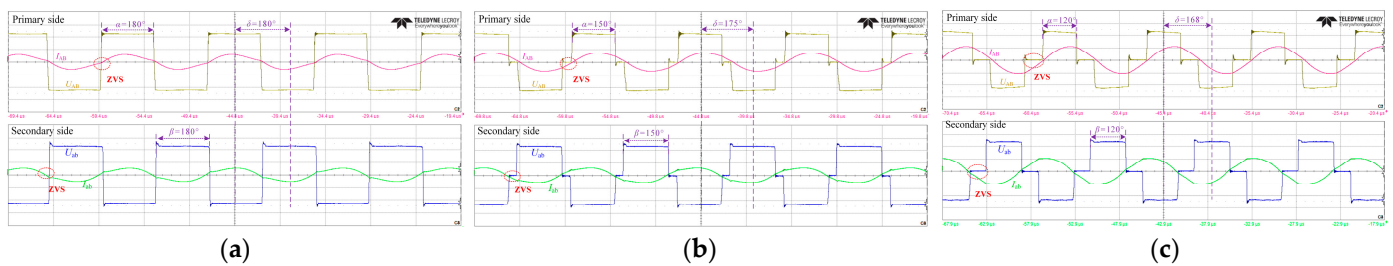


Figure 15. Voltage and current waveforms of the transmitting and receiving side bridges for $k = 0.216$ and $G_{ac} = 1$ at (a) light load, (b) middle load, and (c) full load.

Furthermore, the ZVS operating range of the BIPT system with a misalignment state was tested. Additionally, the experimental waveforms under different loads are given, as shown in Figure 16. As the load changes, by controlling the compensation phase angle $\Delta\delta$, the MOSFETs on both sides can also achieve ZVS operation at $k = 0.237$. Therefore, with the proposed TPSC strategy, the ZVS operating range of the MOSFETs of the converters on both sides can be achieved over a wide load variation range and coupling coefficient. However, it can be seen from Figure 16c that the larger $\Delta\delta$ can fully discharge the parallel parasitic capacitance between the source and drain during the dead time, making the MOSFETs achieve ZVS. However, the greater the $\Delta\delta$, the greater the reactive power of the system, which puts higher requirements on the VA rate of the MOSFETs. However, it is acceptable that the reactive power loss is relatively small compared with MOSFETs working in a hard switching state.

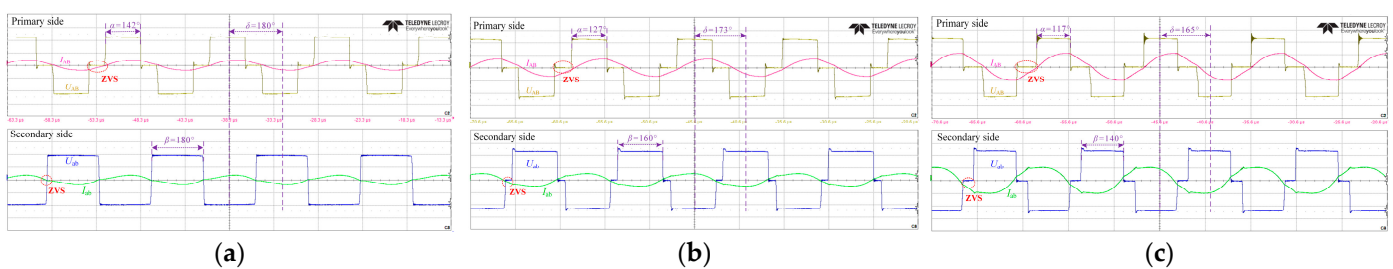


Figure 16. Output voltage and current waveforms of the transmitting and receiving side bridges for $k = 0.237$ and $G_{ac} = 1.1$ at (a) light load, (b) middle load, and (c) full load.

The DC/DC efficiency of the system at various output power levels is presented to substantiate the aforementioned points, as depicted in Figure 17. It is worth noting that the efficiency of the BIPT system is significantly affected under full load conditions when the traditional DPSC strategy is used alone. As can be seen from Figure 17, when BIPT works at 300 W and $k = 0.216$, the system efficiency using only the DPSC strategy is 81.3%, but the system efficiency using the TSPC strategy reaches 88.1%. This is especially evident

when the coupling coefficient increases due to the reduction of the vertical distance because when only the DPSC strategy is used, half of the MOSFETs on both sides cannot achieve soft-switching, which will lead to the amplification of converter losses in the BIPT system. In addition, when the coupling coefficient is reduced due to misalignment tolerance in the horizontal direction, the TPSC strategy proposed in this paper can also be used to reduce the loss of the converter. Specifically, the third phase-shift angle can be increased to make the converters on both sides realize soft switching.

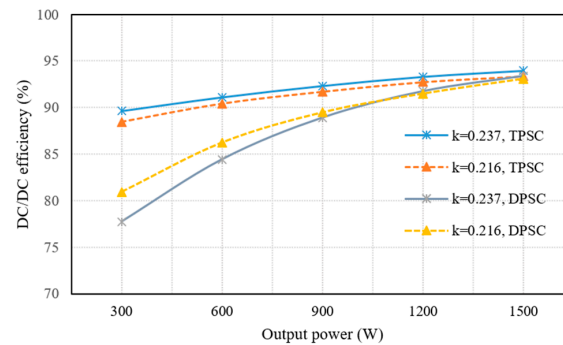


Figure 17. System efficiency against output power under conventional DPSC and TPSC strategies.

After adopting the TPSC strategy, the MOSFETs of the converters on both sides can achieve ZVS operation, significantly improving the system efficiency and reaching a system efficiency of 93.95% at 1.5 kW. It can be seen that compared with the BIPT system loss caused by the hard switching of the conventional DPSC strategy, it is meaningful to adopt the third phase-shift angle δ .

Furthermore, in the case of misalignment, after using the conventional DPSC strategy and the proposed TPSC strategy, the thermal image comparison diagram of the MOSFETs on both sides is given, as shown in Figure 18. Particularly, a FLUKE thermal imager was used to capture thermal images of the MOSFETs on both sides of the converter while the BIPT system was operating at 300 W for 30 min. It can be seen that the temperature of the MOSFETs after adopting the proposed TPSC strategy is lower than that of the conventional DPSC strategy, which indicates that the proposed TPSC strategy can reduce the loss of the BIPT system. Moreover, the highest operational temperature of the MOSFETs utilized in both converter units is lower than 50 °C, and no instances of the over-temperature phenomenon have been observed during operation.

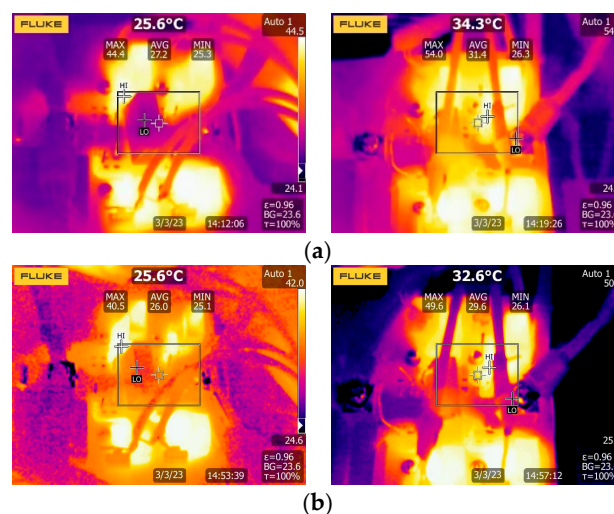


Figure 18. Thermal imaging of the converters of both sides: (a) for the conventional DPSC, (b) for the proposed TPSC.

5. Conclusions

This paper proposes a CVO control strategy that can achieve a wide ZVS range under varying coupling coefficients and loads. Specifically, the CVO characteristics of the DS-LCC compensation resonant network are analyzed. A DPSC strategy is adopted to achieve AC voltage matching to realize a load-independent CVO in a wide range of coupling variations. Furthermore, to broaden the ZVS operating range of the MOSFETs in the converters on both sides, a TPSC strategy based on controlling the phase-shift angle between the full-bridge converters on both sides is proposed. For this reason, a time-domain model is established to describe the voltage and current input and output characteristics of both converters. Through time-domain model analysis, only the conventional DPSC strategy is used, and the system has a narrow ZVS operating range.

On this basis, by adopting the proposed TPSC strategy in the BIPT system. In particular, the proposed TPSC does not require additional DC-DC converters or resonant components, thereby reducing cost and complexity. Based on the proposed TPSC strategy, a 1.5 kW experimental prototype with a variation interval of 100–150 mm was developed for comparison and verification. The experimental results show that the system can achieve a load-independent CVO and wide ZVS operating range under a wide range of coupling coefficient variation, and the measured peak efficiency of the system at 1.5 kW is 93.95%.

Implementing the TPSC strategy in actual electric vehicle charging systems presents multiple challenges. In future work, we will continue to research and enhance the real-time adjustment accuracy of the three-phase-shift angle, further utilizing the TPSC strategy to improve efficiency at higher powers (greater than 1.5 kW).

Author Contributions: Conceptualization, G.L., Y.C. and D.-H.K.; methodology, S.J. and G.L.; validation, J.X. and S.J.; formal analysis, G.L.; investigation, J.X. and S.J.; writing—original draft preparation, G.L.; writing—review and editing, H.Z. and D.-H.K. All authors have read and agreed to the published version of the manuscript.

Funding: This work was supported by the Korea Institute of Energy Technology Evaluation and Planning (KETEP) grant funded by the Korean government (MOTIE) (20225500000120) and in part by the International Scientific and Technological Cooperation Projects in Henan Province under Grant 232102520003, and in part by the General project of Shandong Natural Science and Technology Fund: ZR2022ME214.

Data Availability Statement: Data are contained within the article.

Conflicts of Interest: The authors declare no conflicts of interest.

References

1. Li, Z.; Zhu, C.; Jiang, J.; Song, K.; Wei, G. A 3-kW wireless power transfer system for sightseeing car supercapacitor charge. *IEEE Trans. Power Electron.* **2017**, *32*, 3301–3316. [[CrossRef](#)]
2. Chen, Y.; Zhang, Z.; Yang, B.; Zhang, B.; Fu, L.; He, Z.; Mai, R. A clamp circuit-based inductive power transfer system with reconfigurable rectifier tolerating extensive coupling variations. *IEEE Trans. Power Electron.* **2023**, *39*, 1942–1946. [[CrossRef](#)]
3. Mai, R.K.; Chen, Y.; Li, Y.; Zhang, Y.Y.; Cao, G.Z.; He, Z.Y. Inductive power transfer for massive electric bicycles charging based on hybrid topology switching with a single inverter. *IEEE Trans. Power Electron.* **2017**, *32*, 5897–5906. [[CrossRef](#)]
4. Assaf, T.; Stefanini, C.; Dario, P. Autonomous underwater biorobots: A wireless system for power transfer. *IEEE Robot. Automat. Mag.* **2013**, *20*, 26–32. [[CrossRef](#)]
5. Machnoor, M.; Rodríguez, E.S.G.; Kosta, P.; Stang, J.; Lazzi, G. Analysis and design of a 3-coil wireless power transmission system for biomedical applications. *IEEE Trans. Antennas Propag.* **2019**, *67*, 5012–5024. [[CrossRef](#)]
6. Kan, T.; Mai, R.; Mercier, P.P.; Mi, C.C. Design and analysis of a three-phase wireless charging system for lightweight autonomous underwater vehicles. *IEEE Trans. Power Electron.* **2018**, *33*, 6622–6632. [[CrossRef](#)]
7. Chen, Y.; Kou, Z.; Zhang, Y.; He, Z.; Mai, R.K.; Cao, G. Hybrid topology with configurable charge current and charge voltage output based WPT charger for massive electric bicycles. *IEEE J. Emerg. Sel. Topics Power Electron.* **2018**, *6*, 1581–1594. [[CrossRef](#)]
8. Guo, Y.; Wang, L.; Zhu, Q.; Liao, C.; Li, F. Switch-on modeling and analysis of dynamic wireless charging system used for electric vehicles. *IEEE Trans. Ind. Electron.* **2016**, *63*, 6568–6579. [[CrossRef](#)]
9. Chen, Y.; Zhang, H.; Shin, C.; Jo, C.; Park, S.; Kim, D. An efficiency optimization-based asymmetric tuning method of double-sided LCC compensated WPT system for electric vehicles. *IEEE Trans. Power Electron.* **2020**, *35*, 11475–11487. [[CrossRef](#)]

10. Madawala, U.K.; Thrimawithana, D.J. A bidirectional inductive power interface for electric vehicles in V2G systems. *IEEE Trans. Ind. Electron.* **2011**, *58*, 4789–4796. [[CrossRef](#)]
11. Meins, J.G.; Sinsley, J.D. Method and Apparatus for Supplying Contactless Power. U.S. Patent 6515878 B1, 4 February 2003.
12. Habib, S.; Kamran, M.; Rashid, U. Impact analysis of vehicle-to-grid technology and charging strategies of electric vehicles on distribution networks—A review. *J. Power Sources* **2015**, *277*, 205–214. [[CrossRef](#)]
13. Yilmaz, M.; Krein, P.T. Review of the impact of vehicle-to-grid technologies on distribution systems and utility interfaces. *IEEE Trans. Power Electron.* **2013**, *28*, 5673–5689. [[CrossRef](#)]
14. Zhao, J.; Cai, T.; Duan, S.; Feng, H.; Chen, C.; Zhang, X. A general design method of primary compensation network for dynamic WPT system maintaining stable transmission power. *IEEE Trans. Power Electron.* **2016**, *31*, 8343–8358. [[CrossRef](#)]
15. Dai, X.; Li, X.; Li, Y.; Hu, A.P. Impedance-matching range extension method for maximum power transfer tracking in IPT system. *IEEE Trans. Power Electron.* **2018**, *33*, 4419–4428. [[CrossRef](#)]
16. Li, J.; Zhang, X.; Tong, X. Research and design of misalignment-tolerant LCC–LCC compensated IPT system with constant-current and constant-voltage output. *IEEE Trans. Power Electron.* **2022**, *38*, 1301–1313. [[CrossRef](#)]
17. Zhang, H.; Chen, Y.; Jo, C.H.; Park, S.J.; Kim, D.H. DC-Link and switched capacitor control for varying coupling conditions in inductive power transfer system for unmanned aerial vehicles. *IEEE Trans. Power Electron.* **2021**, *36*, 5108–5120. [[CrossRef](#)]
18. Li, Z.J.; Liu, H.; Huo, Y.; He, J.; Tian, Y.; Liu, J.Q. High-misalignment tolerance wireless charging system for constant power output using dual transmission channels with magnetic flux controlled inductors. *IEEE Trans. Power Electron.* **2022**, *37*, 13930–13945. [[CrossRef](#)]
19. Chen, C.; Zhou, H.; Deng, Q.; Hu, W.; Yu, Y.; Lu, X.; Lai, J. Modeling and decoupled control of inductive power transfer to implement constant current/voltage charging and ZVS operating for electric vehicles. *IEEE Access* **2018**, *6*, 59917–59928. [[CrossRef](#)]
20. Yang, Y.; Zhong, W.; Kiratipongvoot, S.; Tan, S.-C.; Hui, S.Y.R. Dynamic improvement of series–series compensated wireless power transfer systems using discrete sliding mode control. *IEEE Trans. Power Electron.* **2018**, *33*, 6351–6360. [[CrossRef](#)]
21. Gunji, D.; Imura, T.; Fujimoto, H. Operating point setting method for wireless power transfer with constant voltage load. In Proceedings of the IECON 2015–41st Annual Conference of the IEEE Industrial Electronics Society, Yokohama, Japan, 9–12 November 2015; pp. 881–886.
22. Diekhans, T.; De Doncker, R.W. A dual-side controlled inductive power transfer system optimized for large coupling factor variations and partial load. *IEEE Trans. Power Electron.* **2015**, *30*, 6320–6328. [[CrossRef](#)]
23. Colak, K.; Asa, E.; Bojarski, M.; Czarkowski, D.; Onar, O.C. A novel phase-shift control of semibridgeless active rectifier for wireless power transfer. *IEEE Trans. Power Electron.* **2015**, *30*, 6288–6297. [[CrossRef](#)]
24. Mohamed, A.A.S.; Berzoy, A.; Mohammed, O.A. Experimental validation of comprehensive steady-state analytical model of bidirectional WPT system in EVs applications. *IEEE Trans. Veh. Technol.* **2017**, *66*, 5584–5594. [[CrossRef](#)]
25. Liu, Y.; Madawala, U.K.; Mai, R.; He, Z. Zero-phase-angle controlled bidirectional wireless EV charging systems for large coil misalignments. *IEEE Trans. Power Electron.* **2019**, *35*, 5343–5353. [[CrossRef](#)]
26. Nguyen, B.X.; Vilathgamuwa, D.M.; Foo, G.H.B.; Wang, P.; Ong, A.; Madawala, U.K.; Nguyen, T.D. An efficiency optimization scheme for bidirectional inductive power transfer systems. *IEEE Trans. Power Electron.* **2015**, *30*, 6310–6319. [[CrossRef](#)]
27. Jia, S.; Chen, C.; Duan, S.; Chao, Z. Dual-side asymmetrical voltage-cancellation control for bidirectional inductive power transfer systems. *IEEE Trans. Ind. Electron.* **2021**, *68*, 8061–8071. [[CrossRef](#)]
28. Vu, V.B.; Tran, D.H.; Choi, W.J. Implementation of the constant current and constant voltage charge of inductive power transfer systems with the double-sided LCC compensation topology for electric vehicle battery charge applications. *IEEE Trans. Power Electron.* **2018**, *33*, 7398–7410. [[CrossRef](#)]
29. Chen, Y.F.; Wu, J.; Zhang, H.L.; Guo, L.L.; Lu, F.L.; Jin, N.; Kim, D.H. A Parameter tuning method for a double sided LCC compensated IPT system with constant voltage output and efficiency optimization. *IEEE Trans. Power Electron.* **2023**, *38*, 4124–4139. [[CrossRef](#)]
30. Mohamed, A.A.; Berzoy, A.; de Almeida, F.G.; Mohammed, O. Modeling and assessment analysis of various compensation topologies in bidirectional IWPT system for EV applications. *IEEE Trans. Ind. Appl.* **2017**, *53*, 4973–4984. [[CrossRef](#)]
31. Thrimawithana, D.J.; Madawala, U.K.; Neath, M. A synchronization technique for bidirectional IPT systems. *IEEE Trans. Ind. Electron.* **2013**, *60*, 301–309. [[CrossRef](#)]

Disclaimer/Publisher’s Note: The statements, opinions and data contained in all publications are solely those of the individual author(s) and contributor(s) and not of MDPI and/or the editor(s). MDPI and/or the editor(s) disclaim responsibility for any injury to people or property resulting from any ideas, methods, instructions or products referred to in the content.